

ULTRAVIOLET DIVERSITY OF LITTLE RED DOTS AS A PROBE FOR DIRECT-COLLAPSE BLACK HOLE AGES

ELIA CENCI[†], MELANIE HABOUZIT[†], AND DALE D. KOCEVSKI[‡]

[†] Department of Astronomy, University of Geneva, Chemin Pegasi 51, Versoix CH-1290, Switzerland and

[‡] Department of Physics and Astronomy, Colby College, Waterville, 04901, ME, USA

Version June 2, 2026

ABSTRACT

Little Red Dots (LRDs) uncovered by the James Webb Space Telescope have been proposed as candidate galaxies hosting embedded accreting direct-collapse black holes (DCBHs), **yet the relative ultraviolet (UV) emission of their host galaxy remains highly uncertain** and diverse across the population. Using a large-scale cosmological hydrodynamical simulation from the MELI[©]RA suite, we investigate the contribution of PopIII stars and accreting DCBHs in LRD candidates at $z > 8.5$, in the rest-frame $0.2 - 0.6 \mu\text{m}$ band. We find that the UV emission from the host galaxy evolves rapidly over the first ~ 30 Myr following DCBH formation, **reflecting the build-up of stellar mass** and metal enrichment. This evolution consists of a rapid transition from initially BH-dominated systems, with negligible stellar mass, low metallicity, and high accretion rates, to progressively more developed hosts in which rapid star formation enhances the UV output and metallicity increases. After ~ 30 Myr, the stellar continuum typically overwhelms the accreting DCBH contribution, producing bluer colours and more extended stellar distributions. As a result, UV-bright LRDs are predicted to host older DCBHs, have higher gas-phase metallicities, lower BH-to-stellar mass ratios, and lower Eddington ratios. The short-lived nature of the LRD phase places strong constraints on their emergence over cosmic time. Overall, our results suggest that DCBH ages can be constrained from the host galaxy contribution to the UV-optical spectrum of LRDs, relative to that of the accreting DCBH, and support the picture in which a DCBH evolutionary sequence is systematically encoded in emission line properties, gas-phase metallicities, and accretion states.

1. INTRODUCTION

The James Webb Space Telescope (JWST) has uncovered an abundant population of compact, optically red sources dubbed ‘Little Red Dots’ (LRDs; Matthee et al. 2024), in the first billion years of cosmic history ($z \sim 2 - 11$). LRDs are characterised by red rest-optical colours and comparatively blue rest-ultraviolet (UV) slopes, with a ‘V-shaped’ UV-optical continuum inflection around the Balmer limit. Furthermore, LRDs exhibit broad Balmer emission (with FWHM $\gtrsim 2000$ km/s; Greene et al. 2024; Barro et al. 2024; Kocevski et al. 2025; Taylor et al. 2025a), likely tied to faint broad-line active galactic nuclei (AGN) powered by accreting massive black holes (BHs). LRDs are relatively ubiquitous in the early Universe, with a population that outnumbers that of $z < 9$ quasars by an order of magnitude, to then swiftly decline below $z \lesssim 6$ (e.g., Kocevski et al. 2025; Inayoshi 2025; Cenci & Habouzit 2025). To explain their peculiar spectra, commonly invoked scenarios involve either dusty star formation (e.g., Baggen et al. 2024; Barro et al. 2024; Williams et al. 2024) or a reddened AGN (e.g., Onoue et al. 2023; Kocevski et al. 2023; Labbe et al. 2024; Übler et al. 2024; Li et al. 2025a; Volonteri et al. 2025). Alternative explanations for the origin of LRDs include BH-stars (Naidu et al. 2025), quasi-stars (Begelman & Dexter 2026; Roman-Garza et al. 2026), and self-gravitating disks accreting around supermassive stars (Zwick et al. 2025). However, LRDs may not trace a homogeneous population sharing a common physical

origin and appearance, possibly due to varied selection criteria (e.g. Hviding et al. 2025).

Multi-wavelength studies reveal that LRDs are intrinsically X-ray weak (e.g., Ananna et al. 2024; Yue et al. 2024; Tortosa et al. 2026; Rusakov et al. 2026), suggesting either extremely high hydrogen column densities (e.g., Maiolino et al. 2025) or BHs accreting above their Eddington limit (e.g., Inayoshi et al. 2024; Lambrides et al. 2024; Pacucci & Narayan 2024; Madau 2025). Furthermore, LRDs have a clear deficit of both hot and cold dust, disfavoured dust-obscured starbursts as the dominant power source (e.g., Pérez-González et al. 2024; Setton et al. 2025). Recent studies argue that the characteristic turnover around Balmer break wavelengths in LRDs is physically linked to $n = 2$ hydrogen levels rather than to an arbitrary intersection of smooth, unattenuated components (Inayoshi & Maiolino 2025). Individual LRDs further show that dense gas absorption around a strong ionising source can mimic a stellar Balmer break (Naidu et al. 2025; de Graaff et al. 2025; Kokorev et al. 2025; Taylor et al. 2025b).

In general, the relative BH and stellar contributions in LRDs remain uncertain and can vary strongly across the population. Virial methods applied to broad Balmer lines yield BH masses $M_{\text{BH}} \sim 10^{7-9} M_{\odot}$ and moderate Eddington ratios in some datasets (e.g., Greene et al. 2024), while X-ray stacking and population-level spectral analyses favour lower BH masses, $M_{\text{BH}} \sim 10^{6-7} M_{\odot}$, hosted by $\sim 10^{8-9} M_{\odot}$ galaxies and accreting at higher Eddington ratios (e.g., Ananna et al. 2024; Naidu et al. 2025; Sun et al. 2026). Crucially, radiative transfer

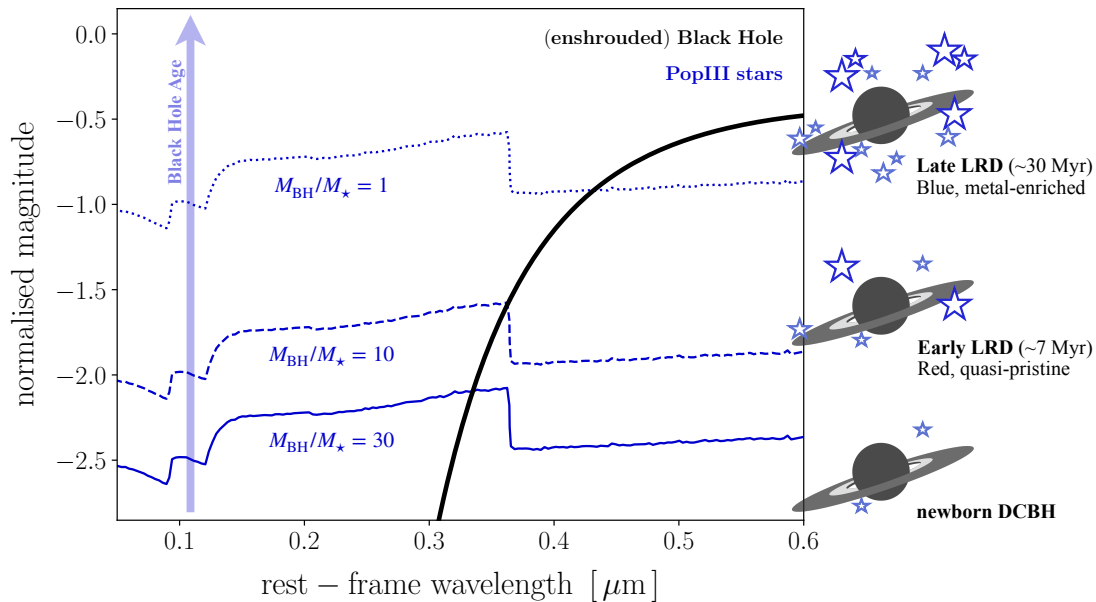


FIG. 1.— Schematic illustration of the evolutionary sequence of LRD candidate DCBHs. We show idealized rest-frame UV-optical composite SEDs of PopIII stars (blue curves) and an enshrouded accreting DCBH (black curve), for different BH-to-stellar mass ratios. Immediately after DCBH formation (early LRD phase), the stellar mass is negligible and the UV continuum is weak, yielding BH-dominated emission and red UV-optical colours. As the system evolves over the first ~ 30 Myr (late LRD phase), rapid star formation increases the stellar UV output, progressively reducing the host-to-core contrast. At later times (> 30 Myr; post-LRD phase), stellar emission dominates the UV-optical SED and the system exits LRD-like colour selection, also exhibiting an extended ($R_* > 100$ pc) stellar mass distribution. The monotonic evolution of the UV-optical balance provides a physically motivated age sequence for high- z LRD candidates and links their observed diversity to different stages of early DCBH growth.

through dense gas can systematically bias standard AGN estimators, with electron scattering and non-virial line broadening implying BH masses well below values derived with virial methods (e.g., Inayoshi & Maiolino 2025; Rusakov et al. 2026). Furthermore, updated corrections on bolometric luminosities may further reduce the inferred contribution from an accreting BH (e.g., Greene et al. 2026). The possible contribution of reprocessed light to the rest-frame optical continuum, and the relation between stellar and dynamical masses can affect the inferred M_{BH}/M_* ratio (e.g., Maiolino et al. 2026; de Graaff et al. 2025; Greene et al. 2026).

Most likely, LRDs represent an heterogeneous population, with substantial diversity in UV slopes, line ratios, and inferred host+core decompositions. The rest-frame UV and optical continua in LRDs may instead trace two physically distinct emission channels: a host component (i.e. emission from stars) dominating the UV, and a compact, reprocessed AGN component dominating the rest-frame optical. Variations in the relative contribution of these two components can generate a sequence of diverse spectra. Recent spectroscopic and panchromatic studies imply that LRDs are likely a heterogeneous population. Using JWST-NIRSpec spectra and available MIRI photometry, Pérez-González et al. (2026) argue that LRDs are spectroscopically heterogeneous and that their UV-optical diversity can be organized primarily as a changing host contribution rather than a single uniform physical class. A similar picture emerges from the diversity of line profiles. Matthee et al. (2026) find that the $H\alpha$ profiles vary systematically with UV-optical colour and strength of the Balmer break: bluer sources have cores with relatively narrow lines, while redder sources show a blue-shifted absorption. Such trends suggest that the continuum diversity is coupled to changes in gas

column density, covering factor, and outflow geometry, rather than being solely a consequence of different stellar population ages or dust reddening. Reported trends between Balmer break strength, absorption features, and diversity of line profiles are qualitatively consistent with this picture (e.g., de Graaff et al. 2025), with increasing [OIII] strength marking the emergence of a more developed, metal-enriched, star-forming host around the AGN.

The physical origin of the first BHs remains a central open problem for modern astrophysics. Heavy seeds channels, such as direct-collapse black holes (DCBHs), provide a plausible theoretical route to rapid early growth, but their predicted observational signatures depend largely on the coupling between accretion physics and the evolving properties of their host galaxy. Major uncertainties in DCBH modelling stem from the stringent environmental requirements for their formation. These include a nearly pristine gas supply, and either intense Lyman-Werner (LW) radiation or sufficiently high mass inflow rates to prevent small-scale fragmentation. By modelling DCBH formation in cosmological hydrodynamical simulations, Cenci & Habouzit (2025) show that the demographics of newly formed DCBHs, set by the physical conditions in their host nursery haloes, can naturally reproduce the observed redshift evolution in the emergence of LRDs (see also Jeon et al. 2026, who reached similar conclusions). In this picture, LRDs correspond to the first 10 – 100 Myr after DCBH formation, during which a residual compact, dense, and quasi-pristine gaseous cocoon both enshrouds the accreting BH and suppresses the escaping X-ray emission. Recent work by Baggen et al. (2026) argues that more than about 40 per cent of LRDs are consistent with having an UV-bright companion at an average projected physical sep-

aration of $\lesssim 5$ kpc. The fraction raises to 85 per cent for the brightest LRDs in their sample. These findings further support the scenario where some LRDs may be associated with young DCBHs, where monolithic collapse is favoured by intense LW flux from the companion.

In this work, we focus on the possibility that a subset of high- z LRDs are young systems hosting newly formed DCBHs. In this scenario, the red optical continuum is primarily associated with an accreting, enshrouded DCBH, while the UV emission is increasingly supplied by the first stellar populations assembling in the host galaxy. The observed UV diversity of LRDs may therefore encode an evolutionary sequence, in which the host contribution grows rapidly during the first few tens of Myr after DCBH formation. We use the MELI \odot RA simulations to test whether the growth of newborn DCBHs and their host galaxies produces a predictable evolution of high- z LRDs.

2. METHODS

The MELI \odot RA suite of simulations aim to implement and test different models for the formation of DCBHs in a cosmological framework, based on local properties of their host haloes and their large-scale environments. In this section, we describe the relevant properties of the one simulation from the MELI \odot RA suite that we use in the present work. We summarize the employed physics models, including our new model for DCBH formation (see Section 2.8). For a more detailed description of the full simulation suite, we refer the reader to upcoming methods papers (Cenci et al., in preparation).

2.1. The Simulation

For this work, we make use of a preliminary run part of the MELI \odot RA suite, consisting of a cosmological volume of $(10 \text{ cMpc})^3$ with periodic boundary conditions, evolved to a provisional final redshift of $z = 8.5$.

Initial conditions are generated at $z = 100$, using the Multi Scale Initial Conditions (MUSIC; Hahn & Abel 2011) code. We assumed cosmological parameters $\Omega_m = 0.272$, $\Omega_\Lambda = 1 - \Omega_m = 0.728$, $\Omega_b = 0.045$, $h = 0.704$, $\sigma_8 = 0.81$, $n_s = 0.967$, that are consistent with results from the Wilkinson Microwave Anisotropy Probe (WMAP-7; measurements taken over 7 years of observations; Komatsu et al. 2011). We employed a Eisenstein & Hu (1998, 1999) transfer function for a cold dark matter cosmology, that includes perturbations due to several baryon effects.

Gravity and hydrodynamics in MELI \odot RA are solved with the adaptive mesh refinement RAMSES code¹ (Teyssier 2002). RAMSES is fundamentally based on a fully threaded oct-tree structure (e.g., Kravtsov et al. 1997; Khokhlov 1998).

The MELI \odot RA simulations start from a minimum refinement level $\ell_{\text{ref,min}} = 9$ (coarse level), corresponding to a coarse resolution of $\Delta x_{\text{max}} \simeq 20$ kpc and a dark matter mass resolution of $m_{\text{DM}} \simeq 2 \times 10^5 M_\odot$. We adaptively refine the grid to a maximum refinement level $\ell_{\text{ref,max}} = 19$, achieving a maximum spatial resolution (i.e., the physical cell size at $\ell_{\text{ref,max}}$) as high as $\Delta x_{\text{min}} \simeq 19$ pc. Refinement is allowed over the entirety

of the simulated volume. The criterion for mesh refinement follows a quasi-Lagrangian approach: for a given cell, refinement is triggered if

$$M_{\text{DM}} + \frac{\Omega_m}{\Omega_b} M_b \geq 8 m_{\text{DM}}, \quad (1)$$

where M_{DM} and M_b are the total dark matter and baryon (gas + stars) mass in the cell, respectively. Additionally, a cell is refined if its size is larger than twice the characteristic Jeans length computed from the cell's temperature and density. Each refinement level consists of a characteristic cell size that is half of that of the previous coarser level. The cells containing sink particles (representing, e.g., BHs) are enforced to get refined to the maximum refinement level that is currently allowed. To keep an approximately constant physical scale-length for grid cells at the finest refinement level, we allow for an additional refinement level (above $\ell_{\text{ref,min}}$) every time the scale factor doubles.

Euler equations for gas dynamics on the grid are solved with an unsplit, second-order MUSCL-Hancock scheme (van Leer 1979) and the Harten-Lax-Van Leer-Contact (HLLC Toro et al. 1994; Toro 1999) approximate Riemann solver. The dynamics of collisionless particles (dark matter, stars, and BHs) is solved for using a particle-mesh (PM) method with cloud-in-cell (CIC) interpolation. Time-steps of finer levels in the mesh hierarchy are updated twice for every update step in the next coarser levels. For stability, time-steps are limited following the Courant–Friedrichs–Lewy condition, with a Courant number of 0.8.

2.2. Clump finder

Haloes in our simulations are associated with gas density clumps, that are identified throughout the simulations with the built-in clump-finder routines of RAMSES (Bleuler & Teyssier 2014; Bleuler et al. 2015). Gas cells with a mass density above the density threshold $\hat{\rho}_{\text{peak}} = 80 \rho_{\text{crit,m}}$ are assigned to the nearest density peak, following the steepest-ascent path. Here $\rho_{\text{crit,m}} = 1.88 \times 10^{-29} \Omega_m h^2 (1+z)^3 [\text{g/cm}^3]$ is the critical matter density of the Universe at the given redshift. Saddle points between peaks, where density is larger than $\hat{\rho}_{\text{saddle}} = 200 \rho_{\text{crit,m}}$, are also identified in order to merge the non-relevant structures to their nearby clumps. When the peak-to-saddle density ratio is below a relevance threshold $\chi_{\text{clump}} = 3$, the peaks are merged together. Otherwise, both peaks survive and are considered as independent clump structures.

2.3. Gas cooling and heating

The equation of state of gas in MELI \odot RA is that of an ideal gas with an adiabatic index $\gamma = 5/3$ (monoatomic gas). Gas cooling follows the model by Sutherland & Dopita (1993), accounting for cooling by H, He, and metals, down to 10^4 K. At temperatures $\lesssim 10^4$ K, we include fine-structure, infrared line cooling through the analytical approximation of the cooling rates by Rosen & Bregman (1995) (based on the results by Dalgarno & McCray 1972). We assume an initial average gas-phase metallicity $Z_0 = 0$. After redshift $z_{\text{reion}} = 8.5$, we consider gas heating from an uniform UV background from high- z reionization sources, following the model by Haardt &

¹ The publicly available repository for RAMSES can be found at: <https://bitbucket.org/rteyssie/ramses/src/master/>.

Madau (1996). In order to mimic the effect of gas heating in star-forming regions, and prevent excessive spurious fragmentation, we impose a polytropic temperature floor $T_{\text{floor}} = T_0 (n/n_{\text{SF}})^{\kappa-1}$ of the high-density interstellar medium, where $\kappa = 1.6$ and $T_0 = 10^3$ K. At high densities, above the density threshold for star formation, n_{SF} , this prescription results in an artificially increased thermal pressure that prevents gas from cooling to lower temperatures (e.g., Springel & Hernquist 2003).

2.4. Star formation

Star formation in MELI \odot RA takes place in gas with hydrogen density above a fixed threshold $n_{\text{SF}} = 1 \text{ cm}^{-3}$. Gas cells that satisfy this density criterion form stars with an expected, average star-formation rate density $\dot{\rho}_*$ following the Schmidt (1959) law:

$$\dot{\rho}_* = \epsilon_{\text{ff}} \frac{\rho}{t_{\text{ff}}}, \quad (2)$$

where ρ is the cell's gas mass density, $t_{\text{ff}} = \sqrt{3\pi/32 G \rho}$ is the local free-fall time, and ϵ_{ff} is the local star formation efficiency per free-fall time. While often taken as a fixed parameter independent of redshift, here ϵ_{ff} is estimated based on the local properties of the interstellar medium, following the turbulence-regulated model by Federrath & Klessen (2012) and Padoan & Nordlund (2011) (see also Hennebelle & Chabrier 2011).

Over a time-step Δt , a gas cell with a $\dot{\rho}_* > 0$ forms a star particle that represents a population of a number N_* of stars, that follows Poisson statistics, and limited such that every gas cell can convert up to a maximum 90 per cent of their available gas mass into stars. The minimum resolved stellar mass in the simulations used in this work is $m_{*,0} \simeq 10^4 M_{\odot}$. The newly formed star particles have a total mass $m_* = N_* m_{*,0}$ and inherit momentum (p_*) and metallicity (Z_*) from their parent gas cell.

Star particles with metallicity $Z/Z_{\odot} < 10^{-4}$ are classified as PopIII stars, whereas PopII stars have larger metallicities (see, e.g., Maio et al. 2011). PopIII stars in MELI \odot RA form with a Salpeter-like initial-mass function (IMF) (Salpeter 1955; Miller & Scalo 1979; Kimm et al. 2017), whereas other stars form with a Kroupa (2001) IMF.

2.5. Stellar feedback

We collectively consider feedback from type II and type Ia supernovae (SNe), that deposit thermal energy, kinetic energy, and metals in the surrounding medium. Furthermore, we distinguish between feedback from PopIII and PopII stars. Star particles that are older than 10 Myr undergo SN explosions that eject a fixed fraction $\eta_{\text{SN}} = 0.2$ of their mass. This is numerically equivalent to assuming that 20 per cent of the stars simultaneously go off as SNe in the coeval population represented by simulated star particles. The ejected mass is instantaneously deposited in the 27 neighbouring father cells, with a metal yield of $Y_{\text{SN}} = 0.1$. Therefore, when triggering SN events, a star particle ejects a mass $M_{\text{ej}} = \eta_{\text{SN}} m_*$, with a metallicity $Z_{\text{ej}} = Z_* + Y_{\text{SN}}(1 - Z_*)$. Furthermore, SNe release a total energy of $E_{\text{SN}} = 10^{51}$ erg per $10 M_{\odot}$ of ejected mass. In our simulations, we do not resolve the radius of SNe remnants at the end of the Sedov–Taylor phase and

the energy (E_{SN}) that is released is instantaneously deposited as thermal energy into nearby gas. In MELI \odot RA, PopIII star particles can go off as SNe after only 3 Myr (approximately the average lifetime for a $40 M_{\odot}$ PopIII star; see Schaerer 2002, 2003). We assume an ejecta mass fraction of $\eta_{\text{SN}} = 0.35$, with a total energy release of 10^{51} erg per $10 M_{\odot}$ of ejected mass and a metal yield of $Y_{\text{SN}} = 0.2$ (see Wise et al. 2012; Kimm et al. 2017, and references therein).

Massive young stars likely reside in dense gas that can efficiently cool, quickly radiating away the thermal energy deposited by SN feedback (e.g., Katz 1992). However, non-thermal processes (e.g., unresolved turbulence, magnetic fields, and cosmic rays) can store additional energy that dissipates over time-scales that are typically longer than the gas cooling time-scale. In order to mimic the effect of non-thermal pressure terms, we turn off the cooling for gas around star particles for a dissipation time-scale $t_{\text{diss}} = 20$ Myr (see, e.g., Gerritsen 1997; Thacker & Couchman 2000; Thacker & Couchman 2001; Stinson et al. 2006; Teyssier et al. 2013), of the order of the lifetime of massive ($> 10 M_{\odot}$) stars. In MELI \odot RA, we use the same dissipation time-scale for both PopII and PopIII star particles.

2.6. Lyman-Werner radiation

The total (unattenuated) Lyman-Werner (LW) flux $J_{\text{LW},i}$ at the centre of the i -th halo is computed accounting for an uniform LW background flux ($J_{\text{LW}}^{\text{bk}}$; following Incatasciato et al. 2023) and the LW flux received from star forming regions around the target halo:

$$J_{\text{LW},i} = J_{\text{LW}}^{\text{bk}} + \sum_n^{\text{stars}} \mathcal{A}_{*,n} \left(\frac{m_{*,n}}{10^3 M_{\odot}} \right) \left(\frac{|\mathbf{r}_i - \mathbf{r}_{*,n}|}{1 \text{ kpc}} \right)^{-2}. \quad (3)$$

Here $m_{*,n}$ and $\mathbf{r}_{*,n}$ are the mass and position vector of the n -th star particle, respectively. The factor $\mathcal{A}_{*,n}$ includes the dimming of the LW flux with increasing stellar age t_* (Schaerer 2003; Lupi et al. 2021). For the n -th star particle, we have:

$$\mathcal{A}_{*,n} = \frac{f_{*,n} \exp[-t_{*,n}/(300 \text{ Myr})]}{[1 + t_{*,n}/(4 \text{ Myr})]^{3/2}}, \quad (4)$$

where $f_{*,n} = 15$ for PopIII stars, and $f_{*,n} = 3$ otherwise (e.g., Greif & Bromm 2006; Agarwal et al. 2014).

We correct the LW fluxes of Equation (3) for attenuation and shielding, by estimating the molecular gas fraction and column density of haloes along the line-of-sight of every source.

2.7. Mass-inflow rates

We estimate the instantaneous mass-flow rate \dot{M}_i onto the central region (where we expect DCBHs to form) of the i -th halo as follows:

$$\dot{M}_{\text{in},i} = - \sum_n \frac{m_n v_{r,n}}{r_n}, \quad (5)$$

where m_n , $v_{r,n}$ and $r_n = |\mathbf{r}_i - \mathbf{r}_n|$ are the mass, radial component of velocity, and distance, respectively, of the gas in the n -th cell, with respect to the centre of the i -th halo.

2.8. Black hole formation

At each time-step, for all haloes identified in a given simulation, we also evaluate the physical conditions around the density peak, within a spherical accretion radius $r_{\text{accr}} = 4 \Delta x_{\text{min}}$, where Δx_{min} is the size of a cell at the highest refinement level in the simulation.

A given halo is considered a candidate DCBH-formation site if all of the following criteria are met:

- The average density, \bar{n} , around the halo's peak exceeds the threshold density for star-formation, n_{SF} : $\bar{n} > n_{\text{SF}}$.
- The average gas-phase metallicity, \bar{Z} , around the halo's peak must be below a defined threshold, Z^{crit} : $\bar{Z} < Z^{\text{crit}}$.
- The effective Lyman-Werner flux, J_{LW} , at the halo's peak must exceed a critical value, $J_{\text{LW}}^{\text{crit}}$: $J_{\text{LW}} > J_{\text{LW}}^{\text{crit}}$.
- The mass-flow rate, \dot{M}_{in} , toward the halo's density peak must exceed a critical value, $\dot{M}_{\text{in}}^{\text{crit}}$: $\dot{M}_{\text{in}} > \dot{M}_{\text{in}}^{\text{crit}}$.
- The halo must not have formed stars: $M_{\star} = 0$.

We do not consider any DCBH formation criterion that evaluates the spin of the dark matter halo, because the halo spin is not clearly coupled to the angular momentum of baryons on smaller scales (e.g., [Dubois et al. 2012b](#); [Bonoli et al. 2014](#)). Furthermore, a low-spin criterion is generally less restrictive compared to requiring a minimum LW flux ([Bhowmick et al. 2022](#)). Different combinations of critical thresholds and criteria are explored in the full suite of MELI \odot RA simulations, with different resolutions and volumes.

2.8.1. Local critical Lyman-Werner flux

Assuming fully neutral (i.e., mean molecular weight $\mu = 1.22$) monoatomic medium (adiabatic index $\gamma = 5/3$) in a virialized halo, we can give an estimate for the local, critical LW flux $J_{\text{LW}}^{\text{crit}}$ above which the LW flux prevents H_2 from efficiently forming in a target halo (see, e.g., [Schauer et al. 2019](#); [Kulkarni et al. 2021](#); [Lupi et al. 2021](#), and references therein):

$$\frac{J_{\text{LW}}^{\text{crit}}}{100 J_{21}} = \epsilon_{\text{H}_2} \left(\frac{1+z}{10} \right)^2 \left(\frac{n}{\text{cm}^{-3}} \right)^2 \left(\frac{M}{10^8 M_{\odot}} \right)^4, \quad (6)$$

where n and M are the average hydrogen density and total mass (dark matter + baryons) of the target halo at redshift z , respectively. Dense-enough haloes in our simulations have masses ranging from approximately 10^6 to $10^{10} M_{\odot}$, implying a vast range of critical LW fluxes. The quantity $\epsilon_{\text{H}_2} = t_{\text{cool,H}_2}^{\text{min}}/t_{\text{H}}$ is the minimum H_2 cooling time-scale $t_{\text{cool,H}_2}^{\text{min}}$ allowed for DCBH formation, in units of the Hubble time-scale t_{H} . In MELI \odot RA, we assume $\epsilon_{\text{H}_2} = 1$. In the simulation used in this work, we

ask the target halo to satisfy $J_{\text{LW}}^{\text{crit}} > J_{\text{LW}}^{\text{crit}}$ to be eligible for DCBH-formation.

2.8.2. Dynamical heating

Dynamical, compressional heating can counteract cooling and prevent H_2 formation for halo mass-growth rates above a local threshold value $\dot{M}_{\text{in}}^{\text{crit}}$ (see, e.g., [Yoshida et al. 2003](#); [Wise et al. 2019](#); [Lupi et al. 2021](#), and references therein). Furthermore, sustained inflow rates onto the central regions of DCBH-forming haloes are required to fuel the accretion of the intermediate protostar phase and overcome the action of radiative feedback (e.g., [Hosokawa et al. 2012, 2013](#); [Schleicher et al. 2013](#); [Chon et al. 2018](#)). Following, e.g., [Lupi et al. \(2021\)](#), for a target halo at redshift z we have:

$$\frac{\dot{M}_{\text{in}}^{\text{crit}}}{M_{\odot}/\text{yr}} = \left(\frac{1+z}{10} \right)^{3/2} \left(\frac{M}{10^8 M_{\odot}} \right)^{-1/2} \left(\frac{J_{\text{LW}}}{J_{\text{LW}}^{\text{crit}}} \right)^{-1}, \quad (7)$$

where n , M , J_{LW} are the average hydrogen density, total mass (dark matter + baryons), and received LW flux of the target halo at redshift z . In order to be considered a candidate DCBH-formation site, the target halo must satisfy $\dot{M}_{\text{in}} > \dot{M}_{\text{in}}^{\text{crit}}$.

2.8.3. Seed mass

The formation sites of DCBHs are expected to experience intense LW flux and mass inflow rates over a finite period of time of a few Myr. To account for this, as well as the accretion phase preceding the collapse of super-massive stars (i.e. the immediate progenitors of DCBH), DCBHs in MELI \odot RA are spawned stochastically in haloes that are eligible for DCBH formation, according to the criteria listed above. At each coarse time-step Δt , we consider a Poisson probability \mathcal{P}_{BH} of forming a DCBH sink particle at the centre of the given halo over that time-step (similarly to, e.g., [Bellovary et al. 2011](#); [Dunn et al. 2018](#)):

$$\mathcal{P}_{\text{BH}} = 1 - \exp(-\Delta t/t_{\text{ff}}), \quad (8)$$

where $t_{\text{ff}} = \sqrt{3\pi/32 G \bar{\rho}}$ is the local free-fall time in the halo. For star-forming gas we have $t_{\text{ff}} \lesssim 70$ Myr. Here $\bar{\rho}$ is the average gas mass density in the cells around the halo centre. We draw a random number $x \in [0, 1]$ from an uniform distribution and, if $x < \mathcal{P}_{\text{BH}}$, we spawn a sink particle representing a new DCBH forming in the simulation. Unlike most state-of-the-art simulations (e.g., Illustris, EAGLE; but see [Habouzit et al. 2017](#)), the seed BHs in MELI \odot RA have a mass $M_{\text{BH}}^{\text{seed}}$, that is determined by the local properties of their host haloes. Specifically, we compute $M_{\text{BH}}^{\text{seed}}$ as a function of the local inflow rate, following the predictions of recent theoretical models (e.g., [Umeda et al. 2016](#); [Haemmerlé et al. 2018](#); [Woods et al. 2017, 2019](#)):

$$\frac{M_{\text{BH}}^{\text{seed}}}{10^5 M_{\odot}} = 2.74 + 2.21 \mathcal{X} + 0.64 \mathcal{X}^2, \quad (9)$$

where we defined:

$$\mathcal{X} = \log_{10} \left[\frac{\langle \dot{M}_{\text{in}} \rangle_{\text{BH}}}{M_{\odot} \text{yr}^{-1}} \right]. \quad (10)$$

Here $\langle \dot{M}_{\text{in}} \rangle_{\text{BH}}$ is the average mass inflow rate in the vicinity of the BH formation site. Around the DCBH formation site, we also spawn a swarm of *cloud* particles, spaced by $\Delta x/2$ and distributed within a sphere of radius $r_{\text{cloud}} = 4\Delta x$, where Δx is the local gas cell size. Cloud particles are implemented purely with a numerical purpose, to probe the average properties of gas surrounding BH particles. With $\langle \cdot \rangle_{\text{BH}}$ we indicate a volume-weighted average computed using a cloud-in-cell (CIC) over the 8 nearest father cells around the sink particle, within r_{cloud} .

2.9. Black hole growth

DCBHs in the MELI@RA simulations grow due to both black hole mergers and gas accretion, which affect the evolution of their mass and spin.

The black hole mass growth rate due to gas accretion is estimated starting from the Bondi-Hoyle-Lyttleton (Hoyle & Lyttleton 1939; Bondi & Hoyle 1944; Bondi 1952) solution:

$$\dot{M}_{\text{B}} = \frac{4\pi G^2 M_{\text{BH}}^2 \langle \rho \rangle_{\text{BH}} / \alpha_{\text{B}}}{\left[|\mathbf{v}_{\text{BH}} - \langle \mathbf{v} \rangle_{\text{BH}}|^2 + \langle c_{\text{s}}^2 \rangle_{\text{BH}} \right]^{3/2}}, \quad (11)$$

where M_{BH} , and \mathbf{v}_{BH} are the black hole mass and velocity, respectively, whereas \mathbf{v} , c_{s} , and ρ are the velocity, sound speed, and mass density of gas in the cells surrounding the sink particle, respectively. With $\langle \cdot \rangle_{\text{BH}}$ we represent the volume-weighted average with CIC interpolation over the 8 nearest father cells around the sink particle, within r_{cloud} . The correction factor α_{B} is introduced to extrapolate the average gas quantities to their value far from the black hole (see Krumholz et al. 2004; Dubois et al. 2010).

Furthermore, we limit the accretion rate \dot{M}_{B} to the Eddington critical accretion rate $\dot{M}_{\text{Edd}} = 4\pi G M_{\text{BH}} m_{\text{H}} / (\epsilon_{\text{r}} \sigma_{\text{T}} c)$, where σ_{T} is the Thomson scattering cross-section, and ϵ_{r} is the radiative efficiency of the accretion process. To summarize, the mass-flow rate towards the black hole is $\dot{M}_{\text{accr}} = \min\{\dot{M}_{\text{B}}, \dot{M}_{\text{Edd}}\}$ and the effective black hole mass-growth rate $\dot{M}_{\text{BH}} = (1 - \epsilon_{\text{r}}) \dot{M}_{\text{accr}}$. Over a time-step Δt , the black hole mass grows by $\dot{M}_{\text{BH}} \Delta t$ and a mass $\dot{M}_{\text{accr}} \Delta t$ is removed from the gas in the cells within r_{accr} from the sink particle. The amount of mass removed from each cell follows the same volume-weighted scheme as the one used to compute average physical quantities in the vicinity of the sink particle.

From the disc mass-flow rate, \dot{M}_{accr} , we can estimate the bolometric luminosity produced in the accretion process as follows:

$$L_{\text{bol}} = \epsilon_{\text{r}} \dot{M}_{\text{accr}} c^2. \quad (12)$$

In this work, we assume an effective radiative efficiency $\epsilon_{\text{r}} = 0.1$ when calculating bolometric luminosities and accretion rates.

2.10. Black hole feedback

We include two modes of BH feedback that are effective in different regimes, characterised by their Eddington ratio $\lambda_{\text{Edd}} \equiv \dot{M}_{\text{accr}} / \dot{M}_{\text{Edd}}$: a ‘radio mode’ for low $\lambda_{\text{Edd}} < 0.01$ and a ‘quasar mode’ for higher λ_{Edd} . In the

quasar mode, we isotropically inject thermal energy into the medium surrounding the BH, at a rate proportional to the BH bolometric luminosity, $\dot{E}_{\text{AGN}} = \epsilon_{\text{q}} L_{\text{bol}}$, with a coupling efficiency $\epsilon_{\text{q}} = 0.1$ (Booth & Schaye 2009; Dubois et al. 2012a). In the radio mode, we transfer momentum to the gas around the BH, as a bipolar outflow with jet velocity of $v_{\text{jet}} = 10^4$ km/s (with a mass-loading factor $\eta_{\text{kin}} = 100$ of the jet on unresolved scales; see, e.g., Omma et al. 2004; Cattaneo & Teyssier 2007; Dubois et al. 2009, 2010). Kinetic energy and momentum are spread over a cone of aperture $\theta_{\text{cone}} = 90$ deg, aligned with the average angular momentum of the gas around the BH.

2.11. SED modelling

We consider a composite spectral energy distribution (SED) consisting of contributions from an accreting DCBH and PopIII stars. The DCBH emission is computed assuming a multi-blackbody spectrum from an optically thick, geometrically thin, α -accretion disc (Shakura & Sunyaev 1973) surrounding a Schwarzschild black hole, given its mass and instantaneous mass-flow rate throughout the disc from the simulation output. The latter is estimated via the accretion rate in Equation (11). The host-galaxy contribution is modelled using zero-age PopIII stars spectra (from Schaerer 2002), for varying DCBH-to-stellar mass ratios from the simulation. We account for effective UV attenuation from Rayleigh scattering with an optical depth (see, e.g., Lee 2013):

$$\tau_{\text{scatt}} = \left(\frac{1216 \text{ \AA}}{\lambda_{\text{rest}}} \right)^4 \left(\frac{N_{\text{HI}}}{4 \times 10^{23} \text{ cm}^{-2}} \right). \quad (13)$$

Furthermore, we consider the following dust extinction law (e.g., Temple et al. 2021):

$$\tau_{\text{dust}} = \frac{A_{\text{V}}}{1.086 R_{\text{V}}} \left[R_{\text{V}} + 6.2 + \left(\frac{800 \text{ \AA}}{\lambda} \right) \right], \quad (14)$$

with an extinction ratio $R_{\text{V}} = 2.7$ (typical value derived for the Small Magellanic Cloud and low-metallicity systems; e.g., Prevot et al. 1984; Calzetti et al. 2000), and visual extinction given by the local neutral hydrogen column density N_{HI} and gas-phase metallicity Z (e.g., Bohlin et al. 1978):

$$A_{\text{V}} = (Z/Z_{\odot}) (N_{\text{HI}} / 1.8 \times 10^{21} \text{ cm}^{-2}). \quad (15)$$

Dust extinction only plays a minor role in the overall attenuation, compared to Rayleigh scattering, for $Z \lesssim 10^{-6} Z_{\odot}$. We assume that the accreting DCBH is enshrouded in a dense reservoir with column density $N_{\text{HI}} \simeq 5 \times 10^{25} \text{ cm}^{-2}$ (similar to, e.g., Pacucci et al. 2026) and pristine gas-phase metallicity $Z \simeq 5 \times 10^{-5} Z_{\odot}$, whereas for PopIII stars we assume they reside in a more diffuse environment with $N_{\text{HI}} \simeq 10^{20} \text{ cm}^{-2}$ and metallicity given by the simulation output (typically, $Z \gtrsim 1 \times 10^{-5} Z_{\odot}$). In this work, we primarily focus on an estimate for the UV-optical colour of our sources given by the emergent luminosity ratio $\Delta \text{mag} = \log_{10} L_{5100} / L_{2500}$, between the emission² at $0.51 \mu\text{m}$ and $0.25 \mu\text{m}$. In our

² With L_{5100} and L_{2500} we indicate the luminosity λL_{λ} evaluated at a wavelength of $\lambda = 5100 \text{ \AA}$ and $\lambda = 2500 \text{ \AA}$, respectively.

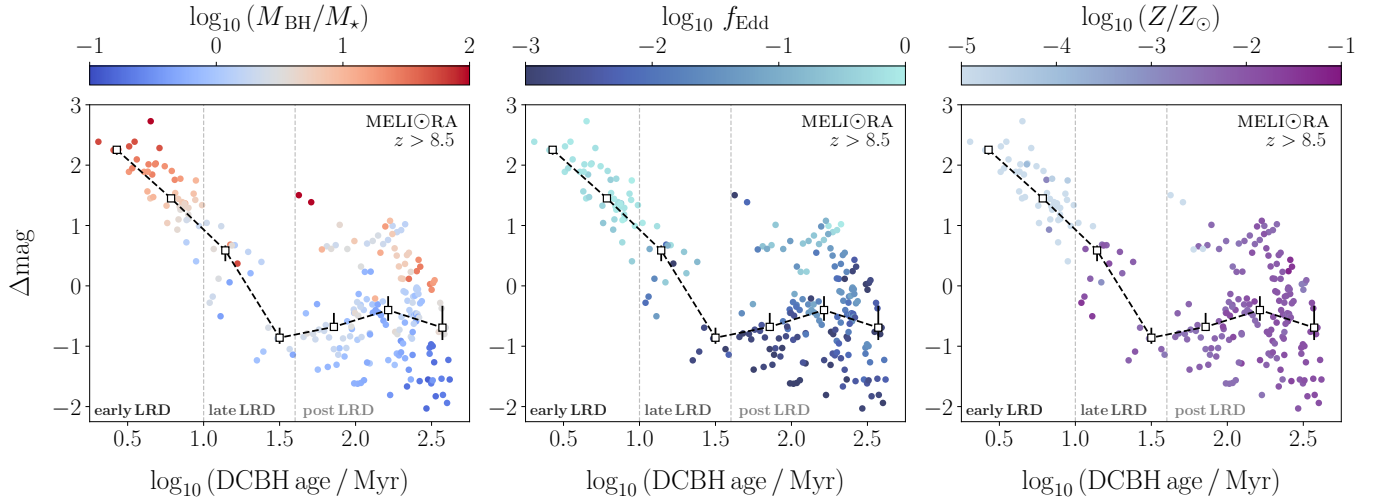


FIG. 2.— Evolution of the UV-optical colour $\Delta\text{mag} = \log_{10} L_{5100}/L_{2500}$ for simulated DCBH+host systems at $z > 8.5$ in MELI@RA, as a function of the DCBH age (time since formation). Here, we only consider accreting DCBHs with bolometric luminosity $L_{\text{bol}} > 10^{40} \text{ erg s}^{-1}$. The black dashed lines trace the median trend of Δmag as a function of DCBH age, with bootstrapped (16th to 84th percentiles) uncertainties. From left to right panels, we colour-code the data points by the BH-to-stellar mass ratio (M_{BH}/M_{\star}), Eddington ratio (f_{Edd}), and gas-phase metallicity (Z). Immediately after the DCBH forms, the UV continuum is weak (high Δmag) because stellar mass is negligible and the accretion flow onto the DCBH is just igniting. As the system ages, sustained star formation rapidly boosts the host’s UV luminosity and promotes metal enrichment, driving a steady decline in Δmag over the first ~ 30 Myr. The rapid evolution of Δmag implies that LRDs associated with newborn DCBHs are necessarily short-lived. In general, the relative UV-to-optical emission provides an age sequence for LRD-candidate DCBHs in their first ~ 30 Myr after their formation.

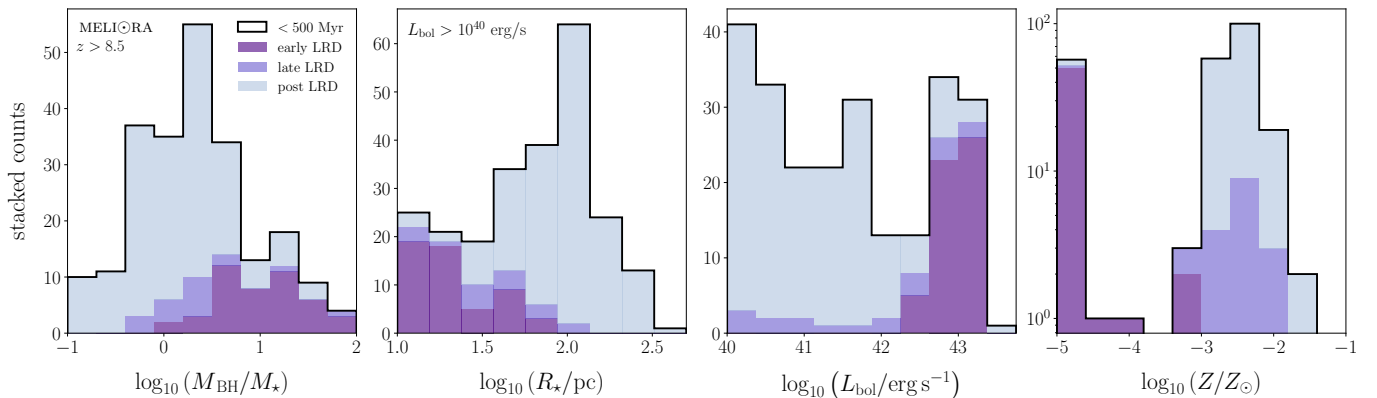


FIG. 3.— Stacked histograms for (from left to right) the BH-to-stellar mass ratio (M_{BH}/M_{\star}), total extent of the stellar mass distribution (R_{\star}), bolometric luminosity (L_{bol}), and gas-phase metallicity (L_{bol}), associated with DCBHs in the early, late, and post LRD phases. Here, we only consider accreting DCBHs with $L_{\text{bol}} > 10^{40} \text{ erg s}^{-1}$. In general, newborn DCBHs in early and late LRDs at $z > 8.5$ in MELI@RA naturally exhibit more compact stellar components, higher bolometric luminosities, and larger BH-to-stellar mass ratios than in post LRDs. As the DCBH ages and stars form within their host galaxy, the BH-to-stellar mass ratio rapidly decreases. Early and late LRDs have sizes below ~ 100 pc, before expanding significantly in the > 30 Myr after DCBH formation. Bolometric luminosities of early and late LRDs are often as high as $\sim 10^{43} \text{ erg s}^{-1}$, to then decrease with DCBH age.

der to show data for non-LRD candidates in the simulation, where the emission of the DCBH accretion disc is drowned in that of PopIII stars, we separately compute L_{5100} and L_{2500} only accounting for the luminosity of the accretion disc and PopIII stars, respectively. This results in simulated sources with $\Delta\text{mag} < 0$. Although the inclusion of bound-free ($n = 2$) Balmer continuum absorption introduces a more abrupt spectral break near $\lambda_{\text{rest}} \simeq 0.37 \mu\text{m}$, it does not affect our results or conclusions. Emission lines

We focus on the evolution of Δmag in simulated haloes hosting DCBHs in relation to DCBH ages, defined as the time since DCBH formation in the simulation. While the absolute values of Δmag depend on the assumed metallicity and HI column density around the DCBH, the qualitative evolutionary trends remain robust to variations in

these parameters, provided that $N_{\text{HI}} \gtrsim 10^{25} \text{ cm}^{-2}$. Our conclusions are therefore based on the relative evolution of UV-optical colour, whereas a quantitative comparison with observed LRDs will require dedicated calibration.

3. RESULTS

We estimate the relative contribution of PopIII stars and the accreting DCBH in LRD candidates in MELI@RA (at $z > 8.5$), via the colour proxy $\Delta\text{mag} \equiv \log_{10} L_{5100}/L_{2500}$ between the rest-frame emission at $0.51 \mu\text{m}$ and $0.25 \mu\text{m}$. Figure 2 shows the evolution of Δmag as a function of the age of DCBHs in the simulation.

Immediately after DCBH formation, the absence of a significant stellar population results in weak UV emission, while accretion onto the DCBH is already in place,

yielding large Δmag values. As the system evolves over the first few Myr, sustained star formation rapidly enhances the UV luminosity, while metal enrichment increases dust opacity and suppresses the direct UV contribution from the AGN, leading to a monotonic decrease in Δmag with BH age. The transition from BH-dominated to host-dominated emission is accompanied by a growing dispersion in Δmag , possibly driven by variations in star formation efficiency, metal production, and accretion histories. Within this framework, we identify three main phases that LRD candidates may undergo:

- (i) **Early LRD phase** (DCBH age < 10 Myr; with median $\Delta\text{mag} \gtrsim 1$ in our model): immediately after DCBH formation; characterised by negligible stellar mass and weak UV emission from the host, pristine low gas-phase metallicities, and high Eddington ratios (possibly super-Eddington) for the accreting DCBH.
- (ii) **Late LRD phase** ($10 \text{ Myr} < \text{DCBH age} < 30 \text{ Myr}$; with median $1 \gtrsim \Delta\text{mag} \gtrsim 0$ in our model): sustained star formation rapidly increases the UV luminosity of the host, while progressive metal enrichment enhances dust opacity. This phase is characterized by declining Eddington ratios, decreasing BH-to-stellar mass ratios of order unity, and rising gas-phase metallicities.
- (iii) **Post LRD phase** (DCBH age > 30 Myr; with median $\Delta\text{mag} \lesssim 0$ in our model): the stellar population dominates the UV output, while the accreting DCBH contributes primarily at longer wavelengths. In this regime, Δmag can reach much lower values and the system eventually no longer satisfies the conditions required for LRD selection. These objects represent a more evolved stage of early DCBH growth.

In Figure 3, we show the stacked histograms of the BH-to-stellar mass ratios, sizes of the stellar component, bolometric luminosities, and gas-phase metallicities, for DCBHs at $z > 8.5$ in MELIORA, for the three different LRD phases defined above. Overall, the increasing contribution of the host galaxy, as measured by the decreasing BH-to-stellar mass ratio from early to post LRDs in MELIORA, is associated with: (i) higher metallicities, primarily due to enrichment from PopIII stellar evolution; (ii) reduced bolometric luminosities for the accreting black hole, as a result of BH feedback; (iii) increased sizes of the stellar component, that become larger than the characteristic ~ 100 pc size of LRDs.

We predict that LRDs with strong UV emission trace a more evolved phase of early BH growth, while UV-faint systems correspond to younger BHs shortly after formation. These results suggest that the relative UV contribution in LRDs provides a physically motivated observational proxy for DCBH age during the first few tens of Myr of evolution. The rapid evolution of Δmag over $\lesssim 30$ Myr implies that the LRD phase is intrinsically short-lived (consistent with the findings of Pérez-González et al. 2026), placing strong constraints on both the emergence rate of LRDs and their redshift distribution.

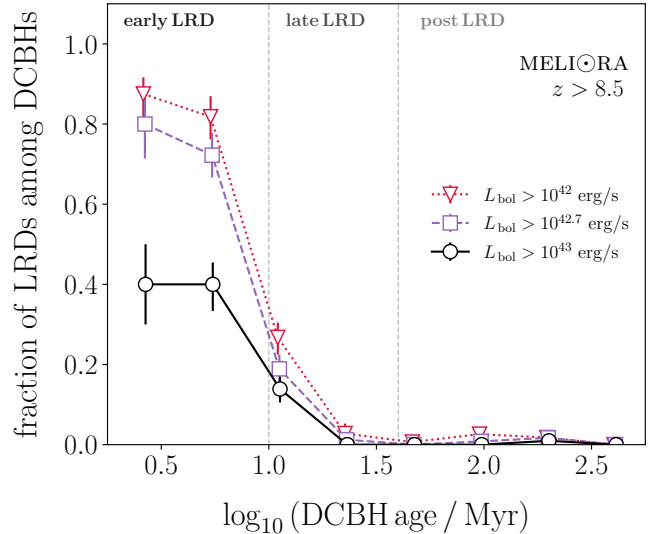


FIG. 4.— Fraction of DCBHs of a given age that are selected as LRD candidates in MELIORA, i.e. that have (i) compact stellar sizes $R_* < 100$ pc, (ii) large UV-optical colours with $\Delta\text{mag} > 0$, and (iii) bolometric luminosity above three different thresholds $L_{\text{bol}} > 10^{42}, 10^{42.7}, 10^{43} \text{ erg s}^{-1}$ (dotted, dashed, and solid lines, respectively). Data points mark the median LRD fraction, with bootstrapped (16th to 84th percentiles) uncertainties. In general, the fraction of LRD candidates selected among newborn DCBHs decreases with DCBH age, consistently reaching zero for ages corresponding to the post-LRD phase.

We perform a linear regression over the combined early+late LRD phases, restricting the sample to DCBHs with ages $t_{\text{BH}} \leq 30$ Myr and $\Delta\text{mag} \geq 0$, and obtain:

$$\log_{10} \frac{t_{\text{BH}}}{\text{Myr}} = -0.27^{+0.04}_{-0.04} \log_{10} \frac{L_{5100}}{L_{2500}} + 1.37^{+0.07}_{-0.06}. \quad (16)$$

Similarly, we find:

$$\log_{10} \frac{M_{\text{BH}}}{M_* L_{\text{bol},43}} = 1.19^{+0.03}_{-0.03} \log_{10} \frac{L_{5100}}{L_{2500}} - 1.75^{+0.08}_{-0.07}, \quad (17)$$

where $L_{\text{bol}} \equiv L_{\text{bol},43} 10^{43} \text{ erg s}^{-1}$. The quoted best-fitting (median) parameters and uncertainties (16th–84th percentiles) are obtained via bootstrap resampling over individual DCBH histories, such that each bootstrap realisation removes or resamples entire BH evolutionary tracks rather than individual snapshots. The combined BH+stellar luminosities are computed assuming a dust attenuation and scattering model; however, our results are sensitive to the specific choice of dust law and column density. The most robust use of the relations above is likely differential rather than absolute: LRDs with larger L_{5100}/L_{2500} should preferentially correspond to younger and more BH-dominated systems, while the more UV-bright sources should trace later stages in which the stellar component has grown.

The abundance of newborn DCBHs (DCBH ages $\lesssim 100$ Myr) in MELIORA, at $8 \lesssim z \lesssim 15$, ranges from $10^{-1} - 10^{-3} \text{ cMpc}^{-3}$, depending on the specific DCBH formation model employed in the simulation (see Cenci & Habouzit 2025). For the simulations used in the present work, the abundance of newborn DCBHs with $L_{\text{bol}} > 10^{40} \text{ erg s}^{-1}$ is about $10^{-3} \text{ cMpc}^{-3}$ at all redshifts $z \lesssim 15$. In Figure 4 shows the fraction of DCBHs of a given age that are selected as LRD can-

didates in MELI \odot RA, i.e. that have (i) compact stellar sizes $R_* < 100$ pc, (ii) large UV-optical colours with $\Delta\text{mag} > 0$, and (iii) bolometric luminosity above three given thresholds $L_{\text{bol}} > 10^{42}, 10^{42.7}, 10^{43}$ erg s $^{-1}$. In general, the fraction of LRD candidates selected among newborn DCBHs steeply decreases with DCBH age, from about 90 per cent (40 per cent) for early LRDs, to $\lesssim 20$ per cent ($\lesssim 10$ per cent) for late LRDs, with a bolometric luminosity threshold of 10^{42} erg s $^{-1}$ (10^{43} erg s $^{-1}$). Using a threshold $L_{\text{bol}} > 10^{40}$ erg s $^{-1}$ yields an LRD fraction that is qualitatively the same as that with $L_{\text{bol}} > 10^{42}$ erg s $^{-1}$. As a result, DCBH with ages $\lesssim 30$ Myr, with a duty cycle of about 30 per cent for newborn DCBHs, we expect an abundance of about 10^{-4} cMpc $^{-3}$, in line with some reported abundances for LRDs (e.g., Kocevski et al. 2025).

4. DISCUSSION AND CONCLUSIONS

In this work, we use the MELI \odot RA cosmological simulations to explore whether young, accreting DCBHs and their host galaxies can reproduce the UV-optical diversity of high- z LRD candidates. In the following, we summarize the main implications of this scenario and highlight its key caveats, observational predictions, and future tests.

4.1. BH-to-stellar mass ratios

Newborn DCBHs in our model are expected to have very high BH-to-stellar mass ratios, because the seed forms before the host has assembled a substantial stellar component. This makes our scenario most applicable to the youngest and most BH-dominated subset of LRDs, rather than to the full observed population. Systems with large inferred stellar masses or low M_{BH}/M_* ratios may instead correspond to, e.g., later evolutionary stages or different seeding channels.

The inferred BH-to-stellar mass ratios of LRDs remain debated, but some recent studies point toward at least a sub-population of LRDs with overmassive BHs relative to their hosts (e.g., Jones et al. 2025; Juodžbalis et al. 2025; Li et al. 2025b; Matthee et al. 2025). These measurements are particularly relevant for heavy-seed models, although they remain sensitive to virial mass calibrations, AGN-host decompositions, and assumptions about the origin of the broad-line widths. Recent stacked-SED analyses (e.g., Pérez-González et al. 2026) suggest a range of host/AGN ratios, indicating significant diversity and selection biases in LRD samples. Heavy-seed (such as DCBH) models predict extreme early BH dominance, but their brief lifetimes and obscuring cocoons make them rare and hard to identify.

4.2. SED modelling

Pérez-González et al. (2026) interpret LRDs as compact galaxies hosting an intermediate-mass BH (within the theoretical DCBH mass range) together with an intense starburst. Their SED modelling combines stellar population templates with an AGN component (accretion disc plus dusty torus). They infer BH-to-stellar mass ratios of ~ 1 per cent and report strong broad FeII emission and Wolf-Rayet features, indicative of very young stellar populations embedded in dense gas.

By contrast, Pacucci et al. (2026) model LRDs as isolated DCBHs without any accompanying galaxy, simulate super-critical accretion onto a $10^5 M_\odot$ BH forming in a pristine halo, compute the emergent spectrum via full radiative transfer. The resulting spectrum exhibits a characteristic V-shaped SED with a pronounced Balmer break. Crucially, this model reproduces observed LRD spectra without invoking any stellar contribution, with intrinsically mild dust attenuation and negligible X-ray emission. In this framework, the LRD turnover arises purely from reprocessed AGN light (see also, e.g., Greene et al. 2024; Labbe et al. 2024), with the Balmer break dominated by bound-free absorption and no prominent hot-dust bump. Current observations are insufficient to discriminate between these two broad scenarios. While the models of Pérez-González et al. (2026) and Pacucci et al. (2026) represent rather opposite interpretations for the physical origin of LRDs, they are affected by substantial uncertainties in dust content, the stellar initial-mass function, and the BH accretion state.

Future targeted observations of far-infrared/sub-mm bands, diagnostic nebular-line ratios, and deep X-ray stacking will be essential to break this degeneracy. Our model lies between these two extremes, as we allow for the presence of a stellar component in addition to the prominent contribution from the DCBH. Within our framework, these two interpretations may correspond to different stages of the same early evolutionary sequence. At the earliest times, the DCBH is embedded in a dense, nearly pristine cocoon and the stellar component is negligible, making the system closer to a DCBH-only SED. The host then rapidly contributes to the UV light and metal enrichment, and the system moves toward a mixed AGN+stellar phase. Eventually, the stellar component dominates the UV continuum and the source no longer satisfies the LRDs' colour selection. The SED diversity of LRD may therefore reflect both intrinsic differences between individual objects and rapid time evolution during the first ~ 10 -30 Myr after DCBH formation.

Our SED modelling is deliberately simplified. We do not perform full radiative transfer through a multi-phase, anisotropic medium, nor do we model the detailed geometry of the obscuring gas, nebular emission, resonant absorption, or dust formation. Consequently, the absolute values of L_{5100}/L_{2500} should not be interpreted as precise predictions for observed LRD colours. A quantitative calibration of the proposed DCBH evolutionary sequence will require dedicated radiative transfer and forward-modelling through JWST filters, and we defer this task to future work.

4.3. Interpretation

We propose that, for at least a subset of LRDs, the relative contribution of the host galaxy and the enshrouded accreting BH evolves rapidly during the first ~ 10 -30 Myr after DCBH formation, producing an age sequence encoded in L_{5100}/L_{2500} . Furthermore, this evolution is systematically associated with trends in emission line properties (as reported by, e.g., de Graaff et al. 2025; Matthee et al. 2026), gas-phase metallicities, and BH accretion state.

The earliest LRD phase that we define is intrinsically rare because it lasts only a few Myr. However, the probability that a DCBH is selected as an LRD may be high-

est during this short interval, when the DCBH is still embedded in the compact gas reservoir associated with the DCBH formation event and the stellar UV contribution remains weak. Later stages can last longer, but the growing host galaxy progressively dilutes the red AGN continuum and lowers the probability of satisfying strict LRD colour and morphology cuts. While older systems naturally move toward mixed AGN+stellar interpretations, earlier LRDs may resemble the DCBH-only spectra proposed by [Pacucci et al. \(2026\)](#), with prominent Balmer breaks and weak nebular emission (as observed in sources like, e.g., [Naidu et al. 2025](#)). Finally, some of the compact, UV-bright descendants of early LRD systems (in their late or post LRD phases) could be naturally associated with the population of so-called Little Blue Dots (LBDs [Brazzini et al. 2026](#)).

Merger-driven BH formation channels may produce heavy seeds in environments that are already enriched and dynamically complex (e.g., [Mayer & Bonoli 2019](#); [Mayer et al. 2024](#)). Such systems may still follow a qualitatively similar decline in the AGN contribution as the host grows, but they would not necessarily exhibit the same pristine early phase or metallicity evolution predicted by our simulation.

An important alternative, or complementary, interpretation is that part of the observed LRD diversity is driven by projection effects rather than BH age. If the obscuring medium is clumpy, flattened, or otherwise non-spherically symmetric, different viewing angles can produce different UV-optical colours at fixed intrinsic BH age. This picture is qualitatively consistent with recent interpretations in which LRD spectral diversity reflects variations in the geometry, covering factor, and column density of dense gas around the accreting BH (e.g., [Brazzini et al. 2026](#); [Matthee et al. 2026](#)).

4.4. Future directions

A key future test of our evolutionary picture will be to connect the UV-optical colours of high- z LRDs to their resolved morphology, AGN-host decomposition, and gas-phase metallicity. In our scenario, UV-brighter and bluer

systems should correspond to later stages, in which the stellar component has grown, metal enrichment has progressed, and the host galaxy begins to extend beyond the compact DCBH-forming region. In general, deep JWST imaging could test whether rest frame UV sizes, colour gradients, or the incidence of nearby UV-bright companions correlate with L_{5100}/L_{2500} . Similarly, rest frame optical emission line diagnostics could reveal whether bluer LRDs preferentially show stronger metal lines and higher inferred metallicities, as expected if they trace more evolved host galaxies. Strongly lensed systems are particularly valuable, possibly enabling deep spectroscopy and spatially resolved constraints on the host and AGN components. For instance, recent studies of lensed or magnified LRDs were able to constrain the low gas-phase metallicities of some systems (e.g., [Maiolino et al. 2026](#); [Kokorev et al. 2025](#); [Tripodi et al. 2025](#)).

Since the simulation used in this work is currently evolved only to $z \simeq 8.5$, our conclusions are mostly restricted to the earliest, high- z LRD candidates will need to be extended to lower redshifts. In addition, the currently simulated volume of $(10 \text{ cMpc})^3$ is relatively limited, which may prevent us from sampling the rarest environments and the most massive BHs expected at these epochs. This work should be interpreted as a first exploration of the early phases of DCBH growth in representative high- z environments. Future work carried out as part of the MELIORA simulation project, including larger volumes and evolution to lower redshift, will be essential to assess whether this evolutionary picture can extend to more massive systems and to the broader LRD population at later cosmic times.

ACKNOWLEDGEMENTS

EC thanks everyone at Ecogia, Department of Astronomy of UNIGE, for helpful discussions. MH and EC acknowledge support from the Swiss SNSF Starting Grant (grant no. 218032). The computations were performed at the University of Geneva, using YGGDRASIL HPC service, and at the Department of Astronomy of UNIGE using BONSAI HPC service. All plots were created with the MATPLOTLIB library for visualization with Python ([Hunter 2007](#)).

REFERENCES

- Agarwal B., Dalla Vecchia C., Johnson J. L., Khochfar S., Paardekooper J.-P., 2014, *MNRAS*, **443**, 648
- Ananna T. T., Bogdán Á., Kovács O. E., Natarajan P., Hickox R. C., 2024, *ApJ*, **969**, L18
- Baggen J. F. W., et al., 2024, *ApJ*, **977**, L13
- Baggen J. F. W., Scoggins M. T., van Dokkum P., Haiman Z., Torralba A., Matthee J., 2026, arXiv e-prints, p. arXiv:2602.02702
- Barro G., et al., 2024, *ApJ*, **963**, 128
- Begelman M. C., Dexter J., 2026, *ApJ*, **996**, 48
- Bellovary J., Volonteri M., Governato F., Shen S., Quinn T., Wadsley J., 2011, *ApJ*, **742**, 13
- Bhowmick A. K., Blecha L., Torrey P., Kelley L. Z., Vogelsberger M., Nelson D., Weinberger R., Hernquist L., 2022, *MNRAS*, **510**, 177
- Bleuler A., Teyssier R., 2014, *MNRAS*, **445**, 4015
- Bleuler A., Teyssier R., Carassou S., Martizzi D., 2015, *Computational Astrophysics and Cosmology*, **2**, 5
- Bohlin R. C., Savage B. D., Drake J. F., 1978, *ApJ*, **224**, 132
- Bondi H., 1952, *MNRAS*, **112**, 195
- Bondi H., Hoyle F., 1944, *MNRAS*, **104**, 273
- Bonoli S., Mayer L., Callegari S., 2014, *MNRAS*, **437**, 1576
- Booth C. M., Schaye J., 2009, *MNRAS*, **398**, 53
- Brazzini M., et al., 2026, arXiv e-prints, p. arXiv:2601.22214
- Calzetti D., Armus L., Bohlin R. C., Kinney A. L., Koornneef J., Storchi-Bergmann T., 2000, *ApJ*, **533**, 682
- Cattaneo A., Teyssier R., 2007, *MNRAS*, **376**, 1547
- Cenci E., Habouzit M., 2025, *MNRAS*, **542**, 2597
- Chon S., Hosokawa T., Yoshida N., 2018, *MNRAS*, **475**, 4104
- Dalgarno A., McCray R. A., 1972, *ARA&A*, **10**, 375
- Dubois Y., Devriendt J., Slyz A., Silk J., 2009, *MNRAS*, **399**, L49
- Dubois Y., Devriendt J., Slyz A., Teyssier R., 2010, *MNRAS*, **409**, 985
- Dubois Y., Devriendt J., Slyz A., Teyssier R., 2012a, *MNRAS*, **420**, 2662
- Dubois Y., Pichon C., Haehnelt M., Kimm T., Slyz A., Devriendt J., Pogossyan D., 2012b, *MNRAS*, **423**, 3616
- Dunn G., Bellovary J., Holley-Bockelmann K., Christensen C., Quinn T., 2018, *ApJ*, **861**, 39
- Eisenstein D. J., Hu W., 1998, *ApJ*, **496**, 605
- Eisenstein D. J., Hu W., 1999, *ApJ*, **511**, 5
- Federrath C., Klessen R. S., 2012, *ApJ*, **761**, 156
- Gerritsen J. P. E., 1997, PhD thesis, -
- Greene J. E., et al., 2024, *ApJ*, **964**, 39

- Greene J. E., et al., 2026, *ApJ*, **996**, 129
- Greif T. H., Bromm V., 2006, *MNRAS*, **373**, 128
- Haardt F., Madau P., 1996, *ApJ*, **461**, 20
- Habouzit M., Volonteri M., Dubois Y., 2017, *MNRAS*, **468**, 3935
- Haemmerlé L., Woods T. E., Klessen R. S., Heger A., Whalen D. J., 2018, *MNRAS*, **474**, 2757
- Hahn O., Abel T., 2011, *Monthly Notices of the Royal Astronomical Society*, **415**, 2101
- Hennebelle P., Chabrier G., 2011, *ApJ*, **743**, L29
- Hosokawa T., Omukai K., Yorke H. W., 2012, *ApJ*, **756**, 93
- Hosokawa T., Yorke H. W., Inayoshi K., Omukai K., Yoshida N., 2013, *ApJ*, **778**, 178
- Hoyle F., Lyttleton R. A., 1939, *Proceedings of the Cambridge Philosophical Society*, **35**, 405
- Hunter J. D., 2007, *Computing in Science and Engineering*, **9**, 90
- Hviding R. E., et al., 2025, *arXiv e-prints*, p. [arXiv:2506.05459](https://arxiv.org/abs/2506.05459)
- Inayoshi K., 2025, *ApJ*, **988**, L22
- Inayoshi K., Maiolino R., 2025, *ApJ*, **980**, L27
- Inayoshi K., Kimura S., Noda H., 2024, *arXiv e-prints*, p. [arXiv:2412.03653](https://arxiv.org/abs/2412.03653)
- Incatasciato A., Khochfar S., Oñorbe J., 2023, *MNRAS*, **522**, 330
- Jeon J., et al., 2026, *ApJ*, **998**, 148
- Jones B. L., et al., 2025, *arXiv e-prints*, p. [arXiv:2510.07376](https://arxiv.org/abs/2510.07376)
- Juodžbalis I., et al., 2025, *arXiv e-prints*, p. [arXiv:2508.21748](https://arxiv.org/abs/2508.21748)
- Katz N., 1992, *ApJ*, **391**, 502
- Khokhlov A., 1998, *Journal of Computational Physics*, **143**, 519
- Kim T., Katz H., Haehnelt M., Rosdahl J., Devriendt J., Slyz A., 2017, *MNRAS*, **466**, 4826
- Kocevski D. D., et al., 2023, *ApJ*, **954**, L4
- Kocevski D. D., et al., 2025, *ApJ*, **986**, 126
- Kokorev V., et al., 2025, *arXiv e-prints*, p. [arXiv:2511.07515](https://arxiv.org/abs/2511.07515)
- Komatsu E., et al., 2011, *ApJS*, **192**, 18
- Kravtsov A. V., Klypin A. A., Khokhlov A. M., 1997, *ApJS*, **111**, 73
- Kroupa P., 2001, *MNRAS*, **322**, 231
- Krumholz M. R., McKee C. F., Klein R. I., 2004, *ApJ*, **611**, 399
- Kulkarni M., Visbal E., Bryan G. L., 2021, *ApJ*, **917**, 40
- Labbe I., et al., 2024, *arXiv e-prints*, p. [arXiv:2412.04557](https://arxiv.org/abs/2412.04557)
- Lambrides E., et al., 2024, *arXiv e-prints*, p. [arXiv:2409.13047](https://arxiv.org/abs/2409.13047)
- Lee H.-W., 2013, *ApJ*, **772**, 123
- Li Z., Inayoshi K., Chen K., Ichikawa K., Ho L. C., 2025a, *ApJ*, **980**, 36
- Li J., et al., 2025b, *ApJ*, **981**, 19
- Lupi A., Haiman Z., Volonteri M., 2021, *MNRAS*, **503**, 5046
- Madau P., 2025, *arXiv e-prints*, p. [arXiv:2501.09854](https://arxiv.org/abs/2501.09854)
- Maio U., Khochfar S., Johnson J. L., Ciardi B., 2011, *MNRAS*, **414**, 1145
- Maiolino R., et al., 2025, *MNRAS*, **538**, 1921
- Maiolino R., et al., 2026, *MNRAS*, **548**, staf2109
- Matthee J., et al., 2024, *ApJ*, **963**, 129
- Matthee J., et al., 2025, *ApJ*, **988**, 246
- Matthee J., et al., 2026, *arXiv e-prints*, p. [arXiv:2603.17667](https://arxiv.org/abs/2603.17667)
- Mayer L., Bonoli S., 2019, *Reports on Progress in Physics*, **82**, 016901
- Mayer L., Capelo P. R., Zwick L., Di Matteo T., 2024, *ApJ*, **961**, 76
- Miller G. E., Scalo J. M., 1979, *ApJS*, **41**, 513
- Naidu R. P., et al., 2025, *arXiv e-prints*, p. [arXiv:2503.16596](https://arxiv.org/abs/2503.16596)
- Omma H., Binney J., Bryan G., Slyz A., 2004, *MNRAS*, **348**, 1105
- Onoue M., et al., 2023, *ApJ*, **942**, L17
- Pacucci F., Narayan R., 2024, *ApJ*, **976**, 96
- Pacucci F., Ferrara A., Kocevski D. D., 2026, *arXiv e-prints*, p. [arXiv:2601.14368](https://arxiv.org/abs/2601.14368)
- Padoan P., Nordlund Å., 2011, *ApJ*, **730**, 40
- Pérez-González P. G., et al., 2024, *ApJ*, **968**, 4
- Pérez-González P. G., et al., 2026, *arXiv e-prints*, p. [arXiv:2602.20247](https://arxiv.org/abs/2602.20247)
- Prevot M. L., Lequeux J., Maurice E., Prevot L., Rocca-Volmerange B., 1984, *A&A*, **132**, 389
- Roman-Garza J., Schaerer D., Charbonnel C., Fragos T., Cenci E., Marques-Chaves R., Oesch P., Xiao M., 2026, *arXiv e-prints*, p. [arXiv:2603.21714](https://arxiv.org/abs/2603.21714)
- Rosen A., Bregman J. N., 1995, *ApJ*, **440**, 634
- Rusakov V., et al., 2026, *Nature*, **649**, 574
- Salpeter E. E., 1955, *ApJ*, **121**, 161
- Schaerer D., 2002, *A&A*, **382**, 28
- Schaerer D., 2003, *A&A*, **397**, 527
- Schauer A. T. P., Glover S. C. O., Klessen R. S., Ceverino D., 2019, *MNRAS*, **484**, 3510
- Schleicher D. R. G., Palla F., Ferrara A., Galli D., Latif M., 2013, *A&A*, **558**, A59
- Schmidt M., 1959, *The Astrophysical Journal*, **129**, 243
- Setton D. J., et al., 2025, *ApJ*, **991**, L10
- Shakura N. I., Sunyaev R. A., 1973, *A&A*, **24**, 337
- Springel V., Hernquist L., 2003, *MNRAS*, **339**, 289
- Stinson G., Seth A., Katz N., Wadsley J., Governato F., Quinn T., 2006, *MNRAS*, **373**, 1074
- Sun W. Q., et al., 2026, *arXiv e-prints*, p. [arXiv:2601.20929](https://arxiv.org/abs/2601.20929)
- Sutherland R. S., Dopita M. A., 1993, *ApJS*, **88**, 253
- Taylor A. J., et al., 2025a, *ApJ*, **986**, 165
- Taylor A. J., et al., 2025b, *ApJ*, **989**, L7
- Temple M. J., Hewett P. C., Banerji M., 2021, *MNRAS*, **508**, 737
- Teyssier R., 2002, *A&A*, **385**, 337
- Teyssier R., Pontzen A., Dubois Y., Read J. I., 2013, *MNRAS*, **429**, 3068
- Thacker R. J., Couchman H. M. P., 2000, *ApJ*, **545**, 728
- Thacker R. J., Couchman H. M. P., 2001, *The Astrophysical Journal*, **555**, L17
- Toro E. F., 1999, *The HLL and HLLC Riemann Solvers*. Springer Berlin Heidelberg, Berlin, Heidelberg, pp 315–339, [doi:10.1007/978-3-662-03915-1_10](https://doi.org/10.1007/978-3-662-03915-1_10), https://doi.org/10.1007/978-3-662-03915-1_10
- Toro E. F., Spruce M., Speares W., 1994, *Shock Waves*, **4**, 25
- Tortosa A., Ricci C., Du P., Venturi G., Ho L. C., Li R., Wang J.-M., Berton M., 2026, *arXiv e-prints*, p. [arXiv:2603.10162](https://arxiv.org/abs/2603.10162)
- Tripodi R., et al., 2025, *Nature Communications*, **16**, 9830
- Übler H., et al., 2024, *MNRAS*, **531**, 355
- Umeda H., Hosokawa T., Omukai K., Yoshida N., 2016, *ApJ*, **830**, L34
- Volonteri M., et al., 2025, *A&A*, **695**, A33
- Williams C. C., et al., 2024, *ApJ*, **968**, 34
- Wise J. H., Abel T., Turk M. J., Norman M. L., Smith B. D., 2012, *MNRAS*, **427**, 311
- Wise J. H., Regan J. A., O’Shea B. W., Norman M. L., Downes T. P., Xu H., 2019, *Nature*, **566**, 85
- Woods T. E., Heger A., Whalen D. J., Haemmerlé L., Klessen R. S., 2017, *ApJ*, **842**, L6
- Woods T. E., et al., 2019, *PASA*, **36**, e027
- Yoshida N., Abel T., Hernquist L., Sugiyama N., 2003, *ApJ*, **592**, 645
- Yue M., Eilers A.-C., Ananna T. T., Panagiotou C., Kara E., Miyaji T., 2024, *ApJ*, **974**, L26
- Zwick L., Tiede C., Mayer L., 2025, *arXiv e-prints*, p. [arXiv:2507.22014](https://arxiv.org/abs/2507.22014)
- de Graaff A., et al., 2025, *A&A*, **701**, A168
- van Leer B., 1979, *Journal of Computational Physics*, **32**, 101

provides fast and easy peer review for new papers in the *astro-ph* section of the arXiv, making the reviewing process simpler for authors and referees alike. Learn more at <http://astro.theoj.org>.

This paper was built using the Open Journal of Astrophysics \LaTeX template. The OJA is a journal which